

Supersonic Retro-Propulsion Experimental Design for Computational Fluid Dynamics Model Validation

Scott A. Berry (Scott.A.Berry@NASA.gov, 757-864-5231)
Christopher T. Laws (Christopher.T.Laws@NASA.gov, 757-864-9383)
William L. Kleb, (Bil.Kleb@NASA.gov, 757-864-4364)
Matthew N. Rhode (Matthew.N.Rhode@NASA.gov, 757-864-5252)
NASA Langley Research Center, Hampton, VA 23681

Courtney Spells (Courtney.Spells@NASA.gov, 757-864-1079)
Jacobs Sverdrup, Hampton, VA 23681

Andrew C. Mccrea (Andrew.C.Mccrea@NASA.gov, 757-8644017)
ATK Space Systems, Hampton, VA 23681

Kerry A. Trumble (Kerry.A.Trumble@NASA.gov, 650-604-4973)
NASA Ames Research Center, Moffett Field, CA 94035

Daniel G. Schauerhamer (Daniel.G.Schauerhamer@NASA.gov, 281-483-0528)
Jacobs Technology, Houston, TX 77058

William L. Oberkampff (wloconsulting@gmail.com, 512-240-5560)
Consultant, Austin, TX 78633

Abstract— The development of supersonic retro-propulsion, an enabling technology for heavy payload exploration missions to Mars, is the primary focus for the present paper. A new experimental model, intended to provide computational fluid dynamics model validation data, was recently designed for the Langley Research Center Unitary Plan Wind Tunnel Test Section 2. Pre-test computations were instrumental for sizing and refining the model, over the Mach number range of 2.4 to 4.6, such that tunnel blockage and internal flow separation issues would be minimized. A 5-in diameter 70-deg sphere-cone forebody, which accommodates up to four 4:1 area ratio nozzles, followed by a 10-in long cylindrical aftbody was developed for this study based on the computational results. The model was designed to allow for a large number of surface pressure measurements on the forebody and aftbody. Supplemental data included high-speed Schlieren video and internal pressures and temperatures. The run matrix was developed to allow for the quantification of various sources of experimental uncertainty, such as random errors due to run-to-run variations and bias errors due to flow field or model misalignments. Some preliminary results and observations from the test are presented, although detailed analyses of the data and uncertainties are still on going.

TABLE OF CONTENTS

1. INTRODUCTION	1
2. CFD VALIDATION EXPERIMENTS	2
3. SRP TEST DEVELOPMENT	3
4. PRELIMINARY DATA	10
5. SUMMARY	14
REFERENCES	14
BIOGRAPHY	15

¹ 978-1-4244-7351-9/11/\$26.00 ©2011 IEEE.

² IEEEAC Paper #1499, Updated January 10, 2011.

1. INTRODUCTION

Present capability for entry, descent, and landing (EDL) of small robotic missions to Mars, typified by a landed mass less than a metric ton, is predicated on the use of parachutes for a significant portion of the deceleration required to safely reach the surface. Practically speaking, this approach is not scalable to larger payloads due to physical limits with parachute size, materials, and testing capabilities. A proposed alternate approach is to use propulsive deceleration early in the trajectory, even during supersonic flight (instead of just at the terminal-landing phase). Thus, supersonic retro-propulsion (SRP), or the use of engine thrust directed into the oncoming supersonic freestream flow, is deemed a potentially enabling technology for future large payload missions to Mars. For a manned mission to Mars, the payload would be on the order of 10s of metric tons. SRP is currently one of the focus areas of the EDL project. For further discussions of SRP from a systems analysis and performance perspective, see [1] - [5]. A broader survey of the literature is provided in [6].

To date, only a handful of studies have been conducted for understanding the fluid phenomena associated with the use of SRP and most of those were performed decades ago, for example see [7]. These older studies were typically exploratory in nature, designed to investigate the aerodynamic behavior of various representative Mars EDL SRP configurations. While useful for providing key insights into the complex interaction between a supersonic freestream and an opposing rocket plume, shown notionally in Figure 1 for a single nozzle, the historical reports have not retained enough detail for comparison against modern computational fluid dynamics (CFD) codes [8]. For instance, while static force and moment response characteristics are often reported, the dynamics of the

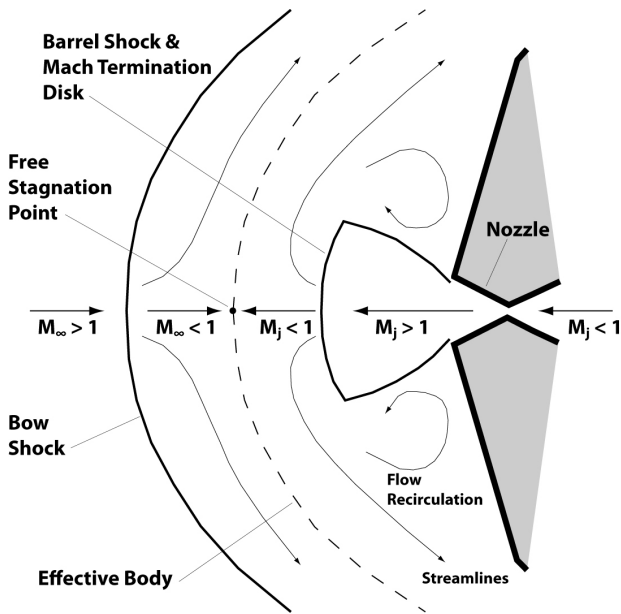


Figure 1 – Conceptual sketch of SRP flow features

interactions are not discussed, nor captured in the still images and time averaged data. A modern SRP experiment, designed specifically for assessing the predictive capability of CFD models, would provide a higher fidelity dataset. From a computational perspective, SRP represents an extremely complex and challenging problem for use as a test case for assessing modeling strengths and weaknesses.

Historically, there has been a heavy reliance on the use of wind tunnels to design and develop most, if not nearly all, flight vehicles - a tradition dating back to the Wright brothers. Recent continuous and systematic advancements in the field of CFD have led many to forecast that most future flight vehicles will be designed with minimal experimental data. For this notion to become reality, CFD codes and results will have to be verified and validated. In the present context, verification refers to the assessment of software and numerical solution algorithm quality, as well as an estimation of the numerical solution error in solving the partial differential equations embodied in the CFD model. Validation refers to model accuracy assessment using comparisons against high fidelity data acquired either from wind tunnel or from flight experiments. This trend towards flight vehicle design based solely on CFD is further discussed in [9], which also provides recommendations on a novel approach to verification and validation (V&V).

The present paper summarizes the design approach for a new experimental SRP study in the Langley Research Center (LaRC) Unitary Plan Wind Tunnel (UPWT). From the onset, this study was deemed primarily a validation experiment in support of improved CFD models and capabilities. As a result, both experimentalists and computationalists were heavily engaged in all aspects of the design of the wind tunnel model and execution of the experiment. For instance, pre-test CFD solutions were instrumental in sizing the model within the tunnel test core to minimize wall effects due to shock reflections. CFD also

highlighted concerns over potential liquefaction within the nozzles of the model, which then led to mitigation strategies for alleviating the need for computing multi-phase flows. On the experimental side, novel approaches for a highly instrumented model design with fast response pressure gages and high speed digital camera systems were selected to allow the monitoring of any high frequency unsteadiness due to the complex fluid structure initiated by SRP. Direct force and moment measurements were deemed to be beyond the scope of the test budget for this initial effort. In addition, tunnel hardware motion was simulated prior to the test to better understand the bounds of model movement within the facility. These simulations allowed the development of a run matrix dedicated to assessing various sources of measurement uncertainty, such as flow field non-uniformity and gage-to-gage repeatability. These aspects will be discussed in further detail in the subsequent sections along with some preliminary data obtained relevant to the overall theme of SRP experimental design.

2. CFD VALIDATION EXPERIMENTS

Traditional experiments can generally be grouped into three broad categories. First, there are discovery type experiments done primarily for improving the fundamental understanding of some physical process. Second, there are model-development or calibration experiments done primarily for constructing or improving a mathematical model of a well understood physical process. Lastly, there are performance, certification, or qualification tests that primarily determine the reliability, performance, or safety of subsystems or complete engineering systems. Conversely, a validation experiment is conducted for the primary purpose of assessing the predictive accuracy of a mathematical model. In other words, a validation experiment is designed, executed, and analyzed for quantitatively determining the ability of a mathematical model expressed in computer software to simulate a well-characterized physical process. Thus, in a validation experiment one could state that *the computational analyst is the customer* or *the code is the customer* for the experiment as opposed to, for example, a physical phenomena researcher, a model builder, or a system project manager.

During the last decade, general guidelines for the design and execution of validation experiments have been put forth in [9] – [11]. The following six validation experiment guidelines were taken from [11]. In the next section of the paper, these guidelines will be related to specific decisions made during the development of the SRP validation experiment.

Guideline 1: A validation experiment should be jointly designed by experimentalists, model developers, code developers, and code users working closely together throughout the program, from inception to documentation, with complete candor about the strengths and weaknesses of each approach.

Guideline 2: A validation experiment should be designed to

capture the essential physics of interest, and measure all relevant physical modeling data, initial and boundary conditions, and system excitation information required by the model.

Guideline 3: A validation experiment should strive to emphasize the inherent synergism that is attainable between computational and experimental approaches.

Guideline 4: Although the experimental design should be developed cooperatively, independence must be maintained in obtaining the computational and experimental system response results.

Guideline 5: Experimental measurements should be made of a hierarchy of system response quantities, for example, from globally integrated quantities to local quantities.

Guideline 6: The experimental design should be constructed to analyze and estimate the components of random (precision) and systematic (bias) experimental uncertainties.

3. SRP TEST DEVELOPMENT

The present SRP wind tunnel effort was proposed from the beginning as a CFD validation experiment. Recognizing the difficulty with extrapolation of Earth-based ground test data to Mars flight conditions, the present effort seeks to assess the accuracy of computational simulations for simple generic configurations in air before progressing to potential Mars flight systems. The intent is to validate and refine CFD models in well-characterized environments before attempting extrapolations to actual flight conditions. A review of the literature reveals that existing experimental SRP data are lacking in critical details such that V&V could not be accomplished without a new test and dataset. A key question underlying this validation experiment is: can CFD replicate the relevant flow features identified from the experiment such that predicted surface quantities can be used to provide an accurate assessment of the forces and moments associated with SRP at flight conditions? To best address this issue, a team of experimentalists and computationalists was formed to foster the design of this experiment, in consideration of the first guideline above.

One of the first decisions for this team was to select an experimental facility. The UPWT was quickly established as an ideal candidate for an exploratory study. This facility provides a wide range of supersonic test conditions, can accommodate a reasonably sized SRP model due to its large test section, and has provisions for a high-pressure air supply essential for studies with blowing. Once the facility was selected, a pre-test CFD study was initiated to help refine the model scale to minimize wall blockage effects. The model was initially selected to be a generic shape with 6-in diameter, as shown in Figure 2, to allow adequate internal volume for the high-pressure air distribution system (capable of providing for multiple nozzle combinations) and instrumentation. The generic shape was selected to be a 70-deg sphere-cone forebody, similar to Viking, with a

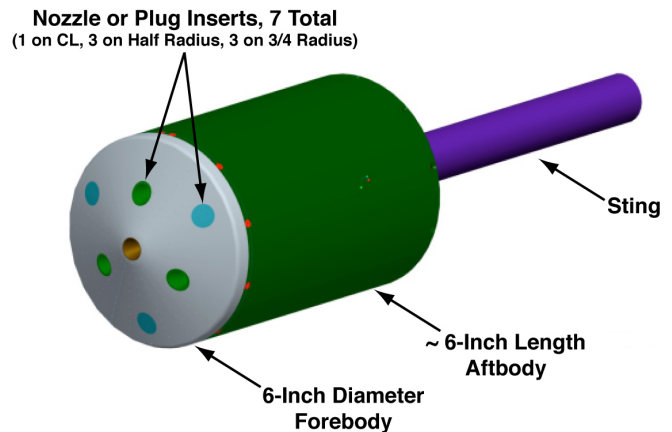


Figure 2 – Oblique view of initial SRP model concept

cylindrical aftbody. Parametric nozzle placement was also desired for this test, so the model centerline, as well as two radial locations, one at $\frac{1}{2}$ the forebody radius and the other at $\frac{3}{4}$, were targeted. As will be shown, the CFD solutions resulted in a resizing of the model, which then reduced the nozzle placement parametrics to one peripheral location. Another concern was to ensure the model's internal characteristics, from both a fluid and thermal perspective, were adequate to ensure a high quality dataset. Finally, the run matrix was developed to provide both the broad parametrics of importance to system designers and allow a quantification of the uncertainties associated with the test. All these aspects will be further discussed in the following sub-sections.

Facility & Test Techniques

The NASA LaRC UPWT is a closed-circuit continuous flow pressure tunnel with two test sections that are nominally 4-ft by 4-ft in cross section and 7 feet long. A photograph of the building that houses this test complex, which was built in 1955, is shown in Figure 3. The primary elements of the UPWT are a 100,000-horsepower compressor-drive system, a dry air supply and evacuating system, a cooling system, and interconnecting tubes that allow air circulation through either of the two test sections. A general layout that highlights these facility elements is illustrated in Figure 4. The Mach number range is approximately 1.50 to 2.86 in



Figure 3 – The Unitary Plan Wind Tunnel complex in Building 1251 at NASA Langley Research Center

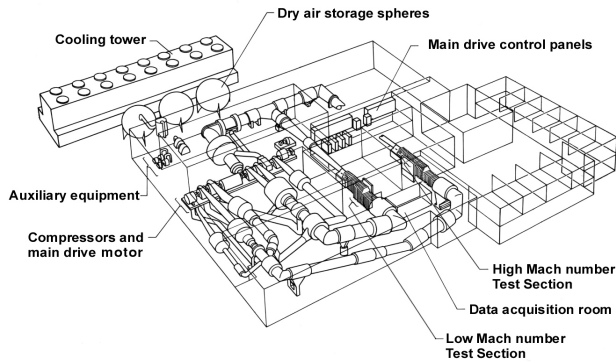


Figure 4 – Schematic of the NASA LaRC Unitary Plan Wind Tunnel complex

Test Section 1 and 2.30 to 4.63 in Test Section 2. The stagnation pressure can be varied up to a maximum of 50 psia in Test Section 1 and 100 psia in Test Section 2. Each test section has an asymmetric sliding-block type nozzle that accelerates the flow to supersonic conditions within the test section. By moving the lower sliding block, the nozzle-throat to test-section area ratio is varied to allow alteration of Mach number. Figure 5 provides a sketch of the sliding-block nozzle concept, while the test section is shown in Figure 6. The second-minimum area downstream of the test section is controlled by hinged sidewalls that provide the required constriction for stabilizing the post-test-section normal shock for the various operating Mach numbers. The most recent calibration of the tunnel (from 1981) is provided in [12], while [13] provides details for planning a test within the UPWT.

Test Section 2 was used exclusively for this study and thus all subsequent facility discussion will focus on the capabilities of this higher Mach number leg. The facility has six centrifugal compressors that are utilized in specific combinations, or modes, depending on the Mach number. For each mode, or Mach number range, the upper limit of the operating envelope is established by the drive system power and the stagnation pressure limit, while the lower limit is dictated by the supersonic-flow stability characteristics at reduced pressure. Typical unit Reynolds numbers for testing in the UPWT Test Section 2 are 1 to 5 million per foot. To allow for the widest range of thrust coefficients ($C_T = T/q_\infty A_{ref}$, where T is the total thrust, q_∞ is freestream dynamic pressure, and A_{ref} is a reference area), only the lowest Reynolds numbers were considered for the present study. The tunnel stagnation temperatures are typically 125 or 150°F depending on the mode of operation.

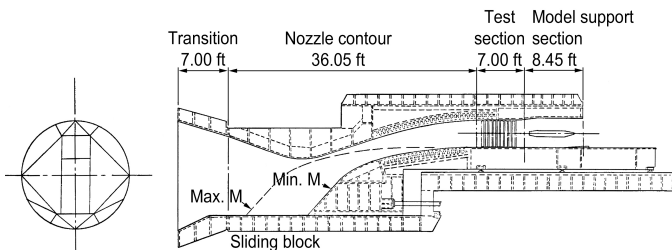


Figure 5 – Schematic of the UPWT Test Section 2 nozzle block

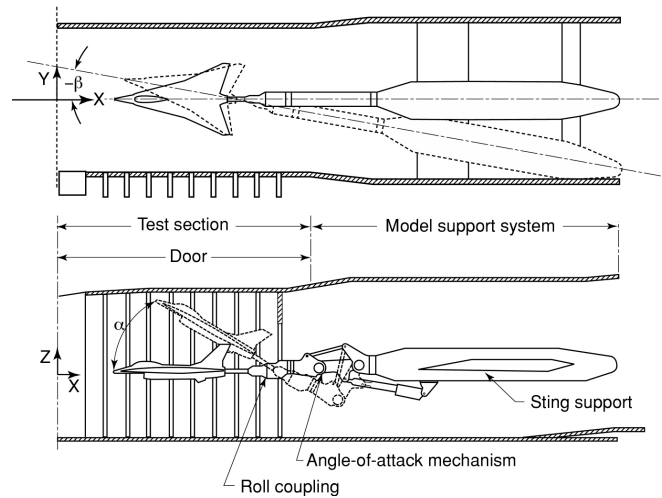


Figure 6 – Test section 2 model support system

Nominal tunnel flow conditions for the range of Mach numbers utilized for this test are provided in Table 1, along with freestream total pressure, temperature, and freestream static pressure and dynamic pressure.

Table 1. Nominal UPWT test section 2 flow conditions

M_∞	Re_∞ (1/ft)	T_{T1} (deg-R)	P_{T1} (psf)	P_1 (psf)	Q_1 (psf)
2.4	1.0E+06	610	814.9	55.7	224.7
3.5	1.0E+06	610	1485.8	19.5	167.0
4.6	1.5E+06	610	3922.1	12.0	177.3

The standard Test Section 2 model mounting hardware was utilized for this test, as shown in Figure 6. The basic mechanism is the horizontal wall-mounted strut that is capable of forward and aft travel (in the x-direction) of 36.25 in. Attached to this strut is a sting support which allows left/right traverse (in the y-direction) and sideslip (β) motion of ± 20 in. and $\pm 14^\circ$, respectively. Forward of the sting support is the angle-of-attack (α) and roll mechanisms which for this study provided pitch motion from -8° to 20° and roll motion of 0° to 180° .

An upgraded capability for supplying high-pressure air to the model has recently been completed for the UPWT. As shown in Figure 7, high-pressure air at nearly 5000 psia is controlled and fed to the model through a digital control valve (DCV). The DCV provides manual control of both

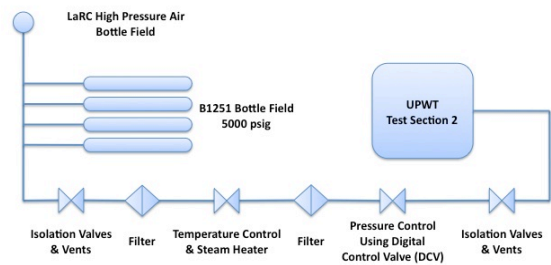


Figure 7 – Simplified schematic of the UPWT high-pressure system

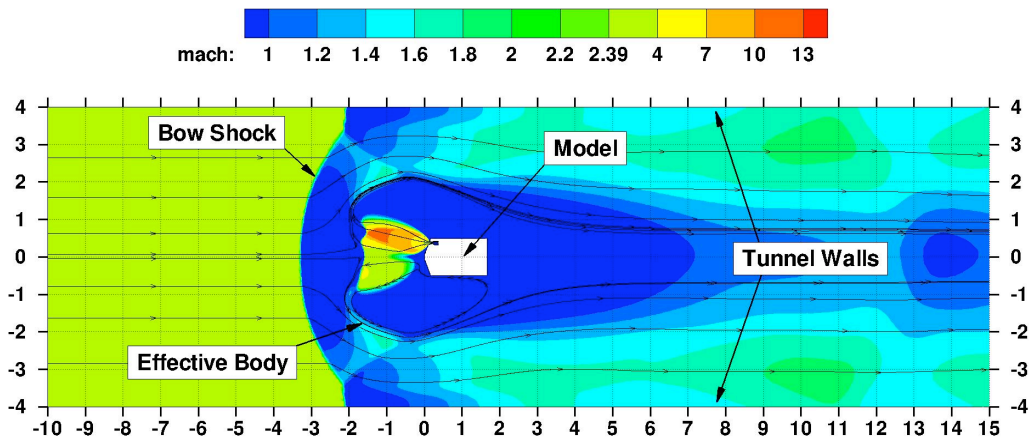


Figure 8 – Potential tunnel blockage predicted for a 6-inch diameter tri-nozzle model at $M=2.4$ and $C_T=10$

temperature (using an inline heater) and pressure. The system design requirements for control of temperature and pressure are ambient to 275°F and 50 to 3800 psia, respectively. The mass flow control range is 0.02 to 30 lb_m/sec at these conditions. Control accuracy is better than $\pm 2\%$ for the pressure range of 50-250 psia, $\pm 1\%$ for the pressure range of 250-3800 psia, and $\pm 5^\circ F$ in temperature.

The large tunnel size and mounting hardware for the UPWT were ideal for allowing adherence to guideline 6, as random and bias uncertainties can be estimated by moving and rolling the model to provide sensor-to-sensor repeatability and measure flow-field nonuniformity.

Pre-Test CFD

The model diameter was initially selected to be 6-in with a capability to host seven nozzles, distributed as shown in Figure 2. A pre-test CFD study was conducted to assess the impact of the increase in effective body size (shown notionally in Figure 1) due to the retro-propulsion exhaust plume and any potential for shock reflections from the sidewalls of the test section that might adversely affect the data. In reference to the guidelines, this is an example of how experimental/computational synergies can be exploited in the early test development stages to increase the

likelihood of obtaining a high fidelity dataset. While only an overview of the pre-test CFD effort is provided here, additional details can be found in [14].

The initial computational results for the 6-in diameter model with flow through the three outermost nozzles showed adverse tunnel wall effects for some of the higher thrust conditions of interest for the test. At the extreme, the preliminary CFD analysis indicated that the tunnel could even “unstart” since large regions within the tunnel were computed to be at subsonic speeds, as shown in Figure 8. For some situations, the effective body diameter, as indicated by the stream surface emanating from the free stagnation point located between the shock and jet termination shock, was predicted to be as high as 3 times larger than the actual body diameter. Subsequently, solutions were requested for a smaller 4-in diameter model for comparison, and these results showed that wall effects were much less likely.

In total, two model diameters were computationally studied for the outer tri-nozzle case for Mach numbers of 2.4, 3.5, and 4.6, angles of attack of 0° , 5° , and 10° , and thrust coefficients of 0, 5, and 10, with and without tunnel walls. From these 108 solutions, 54 plots were made of the difference in surface pressure between “wall” and “no wall”

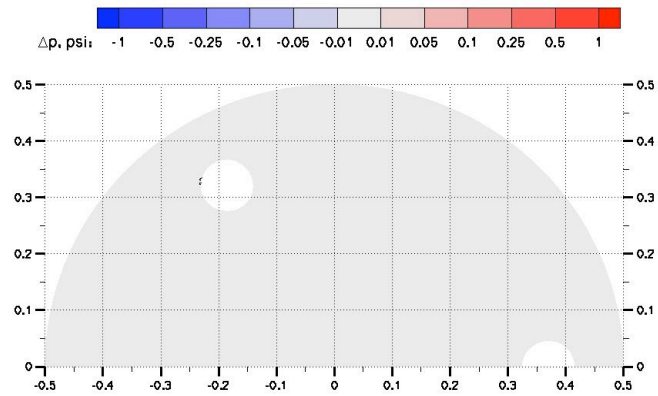


Figure 9a – Difference in forebody surface pressure for 4-in model solutions for $M_\infty = 2.4$, $\alpha = 0^\circ$, and $C_T = 10$ with and without tunnel walls

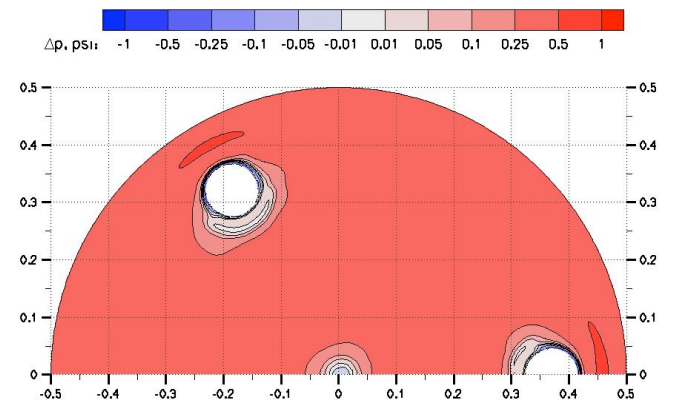


Figure 9b – Difference in forebody surface pressure for 6-in model solutions for $M_\infty = 2.4$, $\alpha = 0^\circ$, and $C_T = 10$ with and without tunnel walls

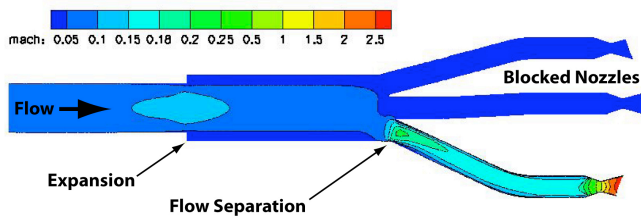


Figure 10 – Mach number contours on the symmetry plane from an internal flow solution for an early plenum and manifold design (with 7 fingers)

cases. Figure 9 shows an example of two such plots for Mach 2.4, zero angle of attack, and C_T of 10. As seen in Figure 9(a), the 4-in diameter model shows no effect of tunnel walls whereas Figure 9(b) clearly shows a substantial change in surface pressure due to the presence of the tunnel walls. Wall interference was considered an unnecessary complication for a CFD validation experiment. Additional results and discussion are provided in [14].

Ultimately, the pre-test CFD solutions led the team to adopt a compromise of a 5-in diameter model due to concerns with trying to fit all the internal components within a 4-in diameter design. The final model design sub-section will provide further detail of the specifics of the internal components. The resizing of the model also resulted in a reduction in scope of the nozzle placement parametrics, as the outer most nozzle set was dropped from further consideration due to packaging concerns of instrumentation wiring around the multi-fingered manifold.

For the model sizing study, the “wall” calculations were completed with inviscid tunnel walls, as no attempt was made to account for the tunnel boundary layer. As will be discussed later, this simplifying assumption turned out to be non-conservative as significant tunnel unsteadiness, which was interpreted as an indicator of an impending tunnel unstart, was observed at C_T as low as 5. In retrospect, this should not have been too surprising as the wall boundary layer in Test Section 2 can be as thick as 8-in [12], which accounts for up to one third of the tunnel’s 4-ft span.

Over the course of the experimental design phase, CFD also influenced several changes to the internal components of the SRP model. For instance, the design of the nozzles and manifold were modified because of internal flow solutions that identified several issues and concerns. The first concern had to do with possible liquefaction within the nozzle plume. Preliminary CFD analysis predicted plume temperatures as low as 10 Kelvin, which is well below the liquefaction temperature for air at the local static pressure. To avoid having to extend the CFD models to include condensation and two-phase flow, which would not be present for hot-gas flight plumes, two adjustments were made to the model design. First, the nozzle area ratio was reduced from 9 to 4 to lower the Mach number at the nozzle exit and thus increase the temperature within the plume. Second, a test requirement was added for heating the plenum gas as high as possible to also increase plume temperatures.

The second concern had to do with the orientation of the off-centerline nozzles. As originally envisioned, the peripheral nozzles were to be “unscarfed,” i.e., mounted perpendicular to the surface of 70-deg slope. Preliminary CFD studies, however, indicated that a 20-deg outward rotation of the nozzle tended to produce larger effective bodies that might further contribute to tunnel blockage effects. To minimize the effective body diameter, the nozzles were aligned parallel to the model axis such that the diverging cone is sliced, or “scarfed,” at a 20-deg angle.

A third issue had to do with flow separations within the nozzles and plenum. To alleviate this concern, radii were added to the throat and plenum corners and the plenum-to-throat convergence angle was reduced from 25 to 20-deg. In addition, the diameter of each nozzle finger was increased to twice the throat diameter to reduce internal flow pressure losses and lower the plenum Mach number. The CFD simulations also underscored the need to round the internal corners at the plenum/manifold junction in order to prevent predicted flow separations downstream of where the outermost nozzle feed lines exited the main plenum chamber as seen in Figure 10. This figure provides a Mach number contour on the symmetry plane for an early plenum/manifold design with seven fingers, one for each of the original nozzle locations (one on centerline, three on the $\frac{1}{2}$ radius, and three on the $\frac{3}{4}$ radius). The center and upper channel on the symmetry plane are plugged and thus no flow is shown. Note that as mentioned earlier, the outermost set of nozzles was eventually dropped from the test plan. These simulations also predicted that the outer portion of the enlarged main plenum chamber served little purpose, as the plenum inlet core flow did not expand to fill it—see Mach 0.05 contour boundary in Figure 10. This result, coupled with packaging constraints, led to the elimination of the sudden expansion and instead utilized gentle flaring to meet the nozzle feed lines (to be shown in a subsequent figure). Finally, these simulations also revealed the importance of heat-soaking the plenum and manifold to avoid large temperature losses to the initially cold walls.

Thermal Considerations

Miniature pressure transducer modules residing within the model was the initial choice for surface instrumentation for this test. By placing the modules within the model, the size and length of the bundle of tubing connecting the surface ports to the module was reduced, thus allowing for a greater number of ports. This choice of module location was not without drawbacks, however. Pressure transducers are rated to work over a limited temperature range, which only became an issue once the decision was made to maximize the plenum temperature to reduce any tendency towards a multi-phase flow from the nozzles. The maximum allowable temperature for the modules chosen for this test was 180°F. The use of a thermal analysis code to better understand the internal model environment for the transducers provides yet another example of the advantage gained from exploiting the inherent synergies between

computational and experimental approaches during test development.

The thermal analysis was done to ensure that the internal model environment would not exceed the temperature constraints of the modules. To do this, the model geometry was imported from the Pro/Engineer CAD design tool and individual parts were modeled in the Thermal Desktop software package [15] to represent the assembly geometry and materials. Radiation, convection, conduction and contact resistance between parts were included. The plenum was set to a fixed temperature, and the thermal analysis code was run to determine the temperatures on the modules. Insulation of various thicknesses was considered to ensure the modules would not exceed their maximum operating temperature. Both quasi-static and transient runs were performed. The primary temperature driver for the pressure transducers was the contact surface between the plenum structure and the module. The use of an insulation barrier between the two was sufficient to keep the module within the allowable temperature range. Details of the chosen insulating material will be discussed in the next section. To monitor the internal model temperatures during the test, thermocouples were located between the insulation and each of the modules. The transient runs showed that as much as 20 minutes of heat soaking was required for the model internal temperatures to approach equilibrium conditions.

Final Model Design & Instrumentation

A sketch of the final design for the 5-in diameter SRP model, a highly instrumented 70-deg sphere-cone forebody with locations for 4 nozzle or plug inserts followed by a cylindrical aftbody, is shown in Figure 11. The assembled model was designed with a partially hollow sting, as shown in cutaway sketch of Figure 12, that feeds an internal plenum connected to each nozzle location via a four-fingered manifold. Note that the final plenum is now a constant diameter pipe (as the sharp corner and step were removed), which includes a 5-deg flare leading to the manifold. The predicted Mach number within the final

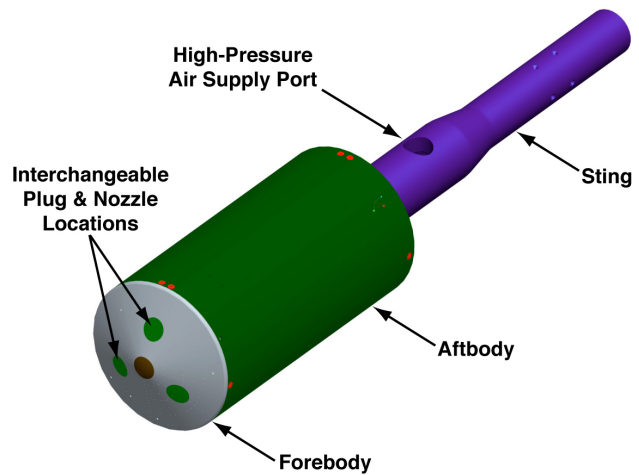


Figure 11 – Oblique view of UPWT SRP model assembly

plenum design is on the order of 0.1 for the worst-case conditions. The sting/plenum/manifold assembly provides the structural load path to hold the forebody with either plugs or nozzles in place. The 10-in long aftbody, which is comprised of two thin half cylinders, provides a non-load bearing enclosure intended to protect the internal instrumentation (also shown in Figure 12). The final nozzle locations are: a single one on the centerline of the model and three equally spaced (120° apart) at the 1/2 radius. The insert locations can host either a 4:1 exit-to-throat area ratio nozzle or plug whose surface is flush to the forebody, providing the baseline configuration. Configuration changes are handled by first removing a side panel and then the forebody is slid forward, without disconnecting the ports, to replace the inserts.

For the insulating barrier between the plenum/sting and the pressure modules, a tough, machinable thermoplastic material called ULTEM® 1000 was selected. This high performance polymer maintains its high strength and rigidity even at elevated temperatures, thus providing an excellent platform with which to attach and thermally isolate the modules. This piece is shown in light green of

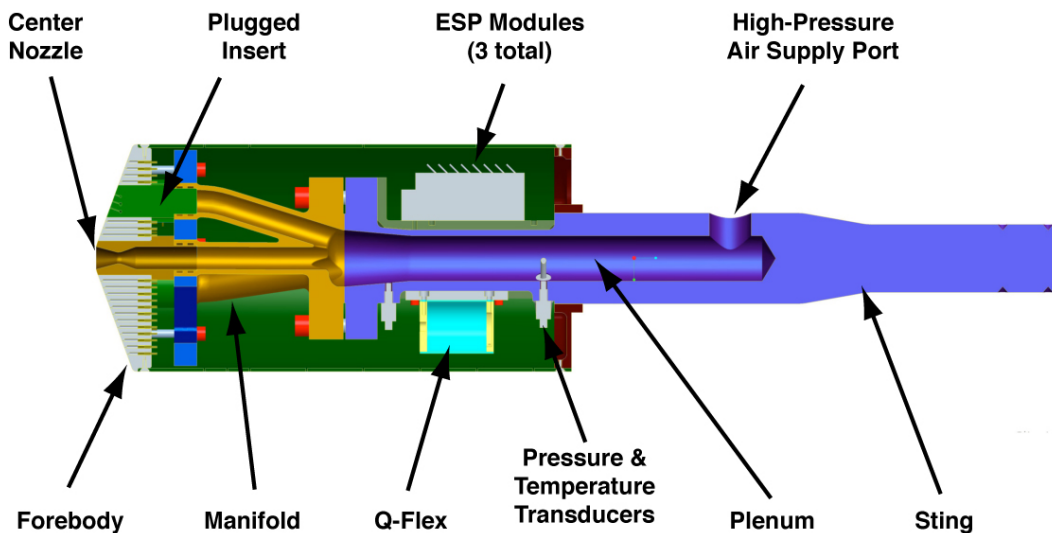


Figure 12 – Section view of the final design UPWT SRP model assembly

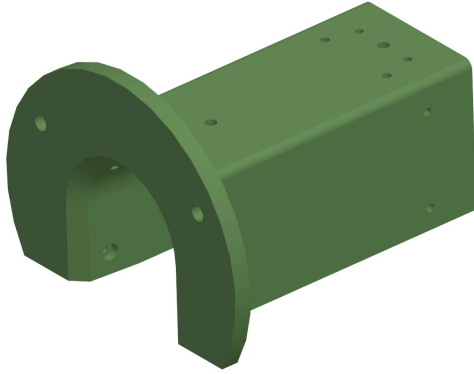


Figure 13 – Oblique view of insulator saddle block

the cutaway of Figure 12. Figure 13 provides an oblique view of the final design of the insulator saddle block showing the mounting holes for assembly. As can be seen, the saddle block provides attachment surfaces for three modules.

The primary measurements on the model consisted of 167 surface pressure ports connected via 0.040-inch-diameter flexible urethane tubing to three Esterline™ electronically-scanned pressure (ESP) transducer modules located onboard the model. Two 64-port modules ($0-5 \pm 0.005$ psid) were used to measure surface static pressures at 118 locations on the model forebody, as shown in Figure 14, as well as 4 locations on the aftbody, while a 48-port ($0-2.5 \pm 0.003$ psid) module was used to measure pressures at the remaining 45 locations on the aftbody. All three modules were teed to a common reference pressure that was pulled down to a hard vacuum to provide absolute pressure measurements. Three separate known pressures were supplied by Ruska Model 6211-801 pressure gages ($0-38 \pm 0.004$ psia) to transducers on each ESP module and were monitored to check for drift in the ESP pressure measurements. In-situ ESP calibrations were performed

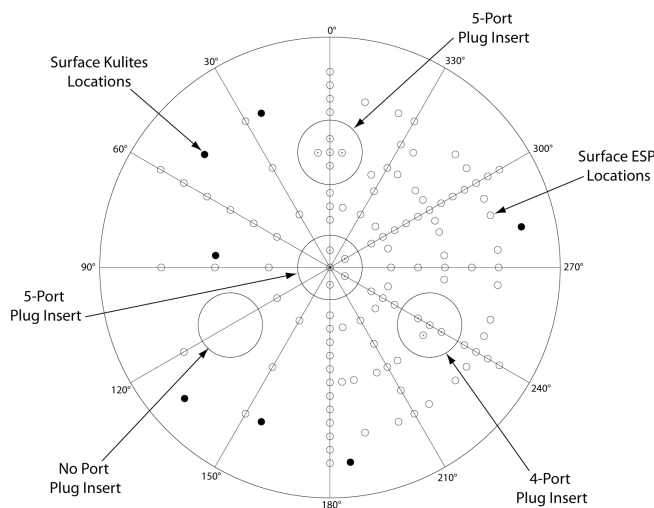


Figure 14 – Forebody surface instrumentation layout for the baseline configuration

using the system Model 8432-15A pressure calibration unit (PCU, $0-15 \pm 0.003$ psia) when the drift exceeded 2.5 psf.

Seven 0.0625-inch-diameter Kulite XCS-062-5A pressure transducers ($0-5 \pm 0.013$ psia) were mounted flush to the surface of the model forebody, also shown in Figure 14, with an adhesive potting material and used for measuring fluctuating surface pressures. Two additional Kulite transducers were mounted in the model aft shell just behind the shoulder but were unfortunately damaged during model assembly. The output signals from the Kulite gages were split to both the standard and high-speed data acquisition systems to provide simultaneous time-averaged and unsteady pressure measurements.

Pressures were measured in the model at different locations along the high-pressure airflow path using up to four Kulite XT-190-2000A pressure transducers ($0-2000 \pm 2$ psia). Two transducers were located at different stations in the model plenum, with the gages mounted flush to the inside surface of the plenum chamber. The remaining pressure transducers were connected to interior surface ports located 0.417 inches upstream of the nozzle inlets for the center nozzle and one of the half-radius nozzles, respectively. Figure 15 provides a representative sketch of the center nozzle also showing the location of the pressure and temperature instrumentation just upstream to the nozzle. These transducers were active only when their respective nozzles were installed in the model. Plenum-flow temperatures were measured using a 6-mm-diameter Omega RTD-NPT-72-A platinum resistance temperature detector (RTD) probe ($132-910 \pm 1$ R) embedded 0.5 inches into the high-pressure airflow (see Fig. 12). Additionally, each of the two instrumented nozzles contained a Type K thermocouple ($132-2742 \pm 4$ R) mounted flush to the inside surface and opposite of the plenum pressure port.

A NASA Langley-built Q-Flex accelerometer was mounted in the model and used to directly measure model pitch angle during the test. The device was calibrated in place as a function of pitch and roll angles using a multi-axis Langley Angle Measurement System (AMS) installed on the model during setup. The resultant calibration accuracy was approximately ± 0.01 degrees.

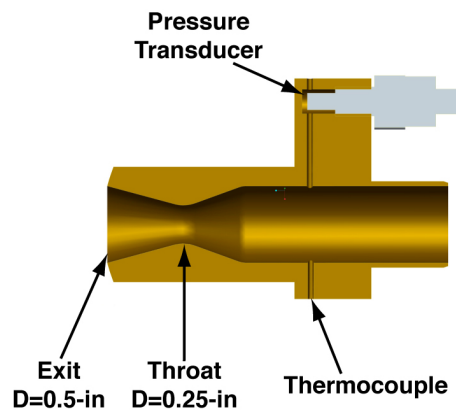


Figure 15 – Close up of the instrumented center nozzle

Eight Type J thermocouples ($492-1842 \pm 4 \text{ R}$) were installed to monitor and measure the thermal environment inside the model during the test. One thermocouple was mounted underneath each ESP module as well as the accelerometer, while the remaining four thermocouples were mounted to the inside surface of the aft shell at a location of approximately half the model length and every 90 degrees around the circumference.

A calibrated Flow-Dyne Engineering subsonic venturi flow meter with a 1.503-inch-diameter inlet and 0.695-inch-diameter throat was installed in the high-pressure air line just outside of the test section and used to measure the mass flow rate of air exhausting through the model nozzles. The venturi inlet pressure was measured using a Druck PDCR 4060 pressure transducer ($0-3000 \pm 2.4 \text{ psia}$), while the inlet temperature was measured using a 0.25-inch-diameter Type T shielded thermocouple probe ($132-1122 \pm 2 \text{ R}$). The pressure drop across the venturi throat was determined with a Bell & Howell Model 4-351-0004 differential pressure transducer ($0-100 \pm 0.05 \text{ psid}$) that was calibrated in one direction to increase accuracy.

To capture the dynamics of flow field interactions between the bow and barrel shocks, a high-speed digital camera was utilized to record Schlieren video. The Phantom 12, from Vision Research, is a 1-megapixel camera capable of taking more than 6200 frames-per-second (fps) at full 1280 x 800 resolution and up to 1,000,000 fps at reduced resolution. For the present test, framing rates between 5,000 and 10,000 fps were utilized.

For this study, an array of instrumentation (with redundancy) has been included to capture all relevant boundary conditions, both steady and unsteady, as suggested by Guideline 2. At the same time, the instrumentation array provides a hierarchy of measured system response quantities (Guideline 5). These are listed from least to most definitive (in terms of quantitative and spatial and temporal resolution): Schlieren photographs, steady state surface and internal pressure measurements, steady state internal temperatures, high speed Schlieren video, and high speed surface and internal pressure measurements.

Model in Tunnel Simulations

To insure that wall interference effects would be kept to a minimum, graphical simulations of the facility hardware were performed to better understand the translation of the model during an α -sweep. The Virtual Diagnostics Interface, or ViDI, methodology [16]-[18] combines two-dimensional image processing, three-dimensional computer graphics, and the handling of large data sets for solving complex aerospace testing and data visualization problems. ViDI was used to simulate for the UPWT hardware over the full range of desired angles of attack and translations within the tunnel, as shown in Figure 16. The primary driver for this analysis was to fully understand the proximity of the model to the tunnel walls and to assess whether wall interference effects would become an issue. The existing

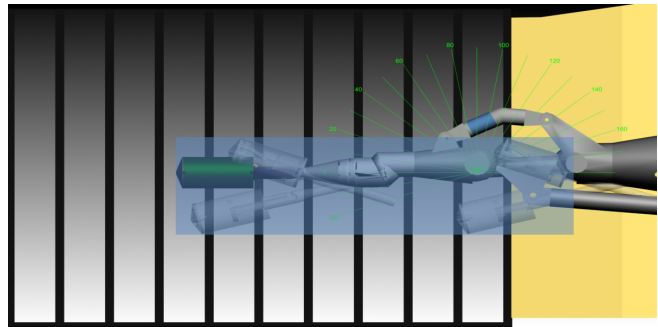


Figure 16 – ViDI simulations showing the extent of model translations during model pitch of -10° to 20°

tunnel hardware provides an angle of attack center-of-rotation such that the model stays within the grey box shown in the figure and thus close to the tunnel centerline for each α . During the test, ViDI was also used for real time data visualization.

Run Matrix Development

Going into the test, there was significant uncertainty about how long configuration changes would take, even though the model was designed with quick disconnects and accessibility in mind. Excessive down time due to model changes would affect the number of runs obtained during the test. Therefore, the run matrix was designed with optimistic expectations for what could be achieved and priorities were assigned such that real time decisions could be made to drop lower priority items if testing appeared behind schedule. With much pre-test debate amongst the team, the matrix was set up with a three-tiered priority system: 1- the highest priority, meaning a “got to have,” 2- a “like to have,” and 3- a “nice to have.” Table 2 provides a summary of the run matrix, showing both the pre-test prioritization and the sequence of parameter variation from first to last. For instance, a complete angle of attack sweep would be completed before incrementing roll. All roll angles would be obtained before any model translations. All translations and/or thrust coefficients would be acquired before changing Mach number. Finally, all Mach numbers were obtained before switching to the next configuration.

The model, as planned and designed, provides for four basic configurations: (1) a baseline model, with all four nozzle insert locations plugged, (2) the center nozzle, with the three peripheral locations plugged (3) the tri-nozzle, with only the center plugged, and (4) the quad-nozzle, with no plugs. The first three configurations were considered Priority 1, while the quad configuration was considered Priority 2. In the end, all four configurations were tested.

For an α -sweep, the tunnel angle of attack mechanism was programmed to pause at -8° , -4° , 0° , 4° , 8° , 12° , 16° , and 20° . This sweep sequence was utilized for most of the test (there were a few cases at the highest angle of attack and thrust coefficients in which the tunnel seemed close to tunnel unstart, so these cases were not acquired).

Table 2. Summary of UPWT SRP run matrix

Testing Sequence	Primary Variable	Pre-Test Priority
Baseline		
1	$\alpha = -8, -4, 0, 4, 8, 12, 16, 20$	1
2	Roll = 0, 60, 120, 180	1
3	X = 40, 25, 50	1
4	Y = 0, -8, 8	1
5	X=25/Y=8, X=50/Y=-8	2
6	Mach = 2.4, 3.5, & 4.6	1
Center Nozzle		
1	$\alpha = -8, -4, 0, 4, 8, 12, 16, 20$	1
2	Roll = 0, 60, 120, 180	1
3	$C_T = 0, 0.25, 0.5, 1, 2, 3$	1
4	X = 40, 25, 50 / Y=0	2
5	X=25/Y=4, X=25/Y=-4	3
6	Mach = 2.4, 3.5, & 4.6	1
Tri Nozzle		
1	$\alpha = -8, -4, 0, 4, 8, 12, 16, 20$	1
2	Roll = 0, 60, 120, 180	1
3	$C_T = 0, 0.5, 1, 2, 3, 4$	1
4	X = 40, 25, 50 / Y=0	2
5	X=25/Y=4, X=25/Y=-4	3
6	Mach = 2.4, 3.5, & 4.6	1
Quad Nozzle		
1	$\alpha = -8, -4, 0, 4, 8, 12, 16, 20$	2
2	Roll = 0, 60, 120, 180	2
3	$C_T = 0, 0.5, 1, 2, 3, 4$	2
4	Mach = 2.4, 3.5, & 4.6	2
Late Repeats - Baseline		
1	$\alpha = -8, -4, 0, 4, 8, 12, 16, 20$	1
2	Roll = 0, 60, 120, 180	1
3	X = 40, 25, 50 / Y=0, -8, 8	2
4	Mach = 2.4, 3.5, & 4.6	1
Late Repeats – Tri Nozzle		
1	$\alpha = -8, -4, 0, 4, 8, 12, 16, 20$	1
2	Roll = 0, 60, 120, 180	1
3	$C_T = 0, 0.5, 1, 2, 3, & 4$	1
4	Mach = 2.4, 3.5, & 4.6	1

Note: Red denotes variables not acquired due to time constraints

To provide greater spatial coverage with the clustered instrumentation, the model was rolled to set angles of 0°, 60°, 120°, and 180°. The roll data was also intended to provide repeatability data with the angle of attack cases (i.e. $\alpha = -4$ with 0° roll is a repeat of $\alpha = 4$ with 180° roll), to help establish flow-field non-uniformity uncertainties.

A full range of streamwise (X) and lateral (Y) model translations were considered important for the uncertainty estimation, especially for the baseline configuration, to provide repeatability data from different stations within the tunnel. For the baseline configuration, independent translations in either X or Y were considered Priority 1 and combined translations in both X and Y were considered Priority 2. For the nozzle configurations, only X translations were considered as Priority 2, while X and Y translations were considered Priority 3.

When nozzles were installed in the model, the plenum pressure was controlled and adjusted via the DCV, with a fixed temperature near 180°F, to provide the thrust coefficients listed in Table 2. Of course, considering the intent of this test, a full range of thrust coefficients was considered a first priority, although additional cases were captured in the matrix as Priority 2, meaning they would be acquired if time were available.

To minimize the number of tunnel conditions for the present test and to maximize thrust coefficient, only the lowest attainable Reynolds number were considered for the full range of Mach numbers. For Mach numbers of 2.4 and 3.5, the Reynolds number was 1×10^6 /ft; while for Mach 4.6, Re_∞ was 1.5×10^6 /ft. The Mach number sweep was considered a first priority.

4. PRELIMINARY DATA

After roughly a six month design and fabrication cycle, the model was ready in time for the scheduled entry into the LaRC UPWT on July 1st, 2010. Although the budget allowed for about a two-week entry into the facility, minor issues stretched the tunnel occupancy time to the entire month of July. All priority 1 objectives were accomplished with the exception of the late test repeat runs on the tri-nozzle configuration. There were also a couple of Priority 2 objectives achieved. Figure 17 provides an installation photo of the tri-nozzle configuration, which shows the tunnel hardware and high-pressure-air line and instrumentation wiring bundles. Note all connections to the model required extra slack to allow a full range of motion



Figure 17 – Installation photo showing the tri-nozzle configuration with high-pressure & instrumentations lines



Figure 18 – Photo showing the internal pressure lines and instrumentation wiring

without binding. Figure 18 provides a photo of the internal volume of the model (with one half of the abody removed) showing the pressure tubing and quick disconnects, and thermocouple wires. Just before installation into the tunnel, a pressure qualification test was performed to 3750 psia, which allowed for safe operating pressures up to 2500 psia. The tunnel, however, had relief valves for their high-pressure system set to 2350 psia.

During the test, model surface pressures measured with the ESP modules were acquired with the Esterline 8400 System at 10 Hz. The remaining data channels were acquired at 30 Hz through a NEFF 620 signal conditioner/multiplexer system. Both systems used a sampling period of 2.5 seconds. All channels were processed through analog 1-Hz, low-pass, 4-pole Butterworth filters and recorded using a MODCOMP 88100 computer at 16-bit analog-to-digital (A/D) conversion. The unsteady pressure data from the Kulite transducers were sampled at 40,000 Hz for a 2.5-second sampling period using a National Instruments/Labview-based high-speed data system synchronized to the standard data system. These data were processed through a 20,000 Hz low-pass filter and recorded at 16-bit A/D conversion.

Raw voltages from the instrumentation were recorded and processed in real time through respective calibration functions into engineering unit values for real-time display, monitoring, and plotting. Facility flow conditions were calculated via standard gas dynamic equations using measured tunnel stagnation conditions and calibrated values of freestream Mach number. These flow conditions were then used to compute parameters such as the surface pressure coefficients, nozzle pressure ratios, nozzle exit-to-static pressure ratios, and nozzle thrust coefficients.

The measured plenum static pressures were corrected to total pressure values using total-to-static pressure ratios calculated from estimates of the plenum Mach number. These estimates were computed from a binomial approximation of the mass flow rate equation using the measured mass flow rates, plenum temperatures, and plenum cross section areas, and are valid for small values of

Mach number. Nozzle exit conditions were calculated based on the plenum total conditions and the nozzle exit-to-throat area ratios. The thrust of each nozzle was computed from the total measured mass flow rates and the ratio of the individual nozzle throat area to the total nozzle throat area.

The model nose position relative to the test section coordinate system was computed for each set-point based on the axial and lateral movements of the model support system as well as the pitch and yaw angles of the model.

The final data are still being processed and assembled for distribution to the team. In observance of Guideline 4, only the tunnel and model flow conditions will be distributed such that experimental and computational results cannot bias each other.

Baseline Data

The baseline configuration runs were primarily dedicated to quantifying various sources of experimental uncertainty. The lateral and streamwise translations to various stations within the tunnel, coupled with the model roll angles allows for sensor-to-sensor comparisons such that instrumentation and flow-field non-uniformity uncertainties can be estimated. In the streamwise direction, the model translations are 15-in forward and 10-in back from the center-point position. In the lateral direction, the model translations are ± 8 -in. This uncertainty assessment task is presently on going.

Figure 19 provides a sample Schlieren image for the baseline configuration at $M_\infty = 2.4$ and $\alpha = 0$ -deg. In this particular case, the model has been translated forward such that the flowfield around the support structure can be visualized. The corresponding comparison of the measured surface pressure from one ray of instrumentation as compared against the pre-test CFD results is shown in Figure 20. This comparison was ViDI generated real-time



Figure 19 – Sample Schlieren image for the baseline configuration at $M_\infty = 2.4$ and $\alpha = 0$ -deg

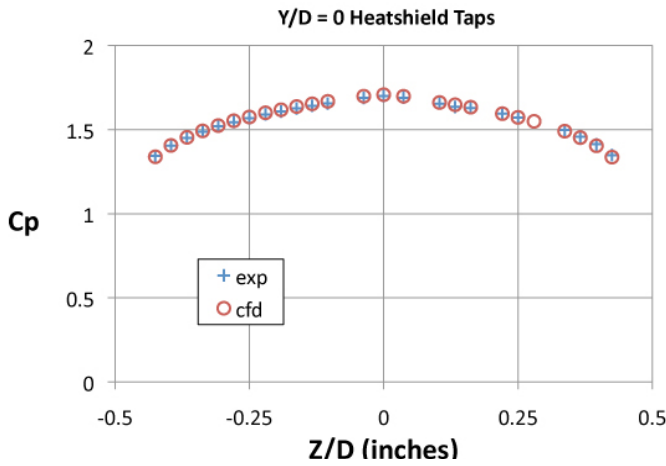


Figure 20 – Sample ViDI “quick-look” comparison of data against pre-test prediction for baseline configuration at $M_\infty=2.4$ and $\alpha = 0$ -deg

during the test to provide a quick look assessment of the quality of data. The as-run conditions for this case closely matched the conditions used for the pre-test solution, making this quick look possible. The excellent agreement provided confidence that the surface instrumentation was behaving as expected, even though the preliminary data shown here has yet to go through the post-test data finalization process. Note that one sensor, located on the outboard plug insert, was known to be bad possibly due to a pinching of the pressure tube and that experimental data point was omitted.

Center Nozzle

The single nozzle configuration provides the simplest nozzle case for the CFD comparisons and the data most comparable to historical information. A few streamwise translation cases were planned but not performed due to time constraints. In addition, many of the 60 and 120-deg roll

cases were dropped also due to time constraints.

A sample Schlieren image for the center nozzle configuration at $M_\infty = 2.4$, $\alpha = 0$ -deg, and $C_T = 1.0$ is shown in Figure 21. As can be seen in the image, the flow emanating from the nozzle forms a classic expansion fan and barrel shock, terminated by a curved Mach disk just behind the bow shock. Even for this relatively low value thrust coefficient of 1.0, the diameter of the Mach disk is nearly as big as the diameter of the model. For the most part, this flow structure appeared mostly steady with the exception of a small amount of unsteadiness seen near the triple points on either side of the Mach disk. This observation is made based on a review of the high-speed video and is not reflected in the sample still image shown. Generally, the center nozzle provided for a mostly steady flow field for angles of attack below 10-deg across the spectrum of Mach numbers and thrust coefficients acquired.



Figure 22 – Sample Schlieren image for the center nozzle configuration at $M_\infty=4.6$, $\alpha = 0$ -deg, and $C_T = 1.0$



Figure 21 – Sample Schlieren image for the center nozzle configuration at $M_\infty=2.4$, $\alpha = 0$ -deg, and $C_T = 1.0$



Figure 23 – Sample Schlieren image for the center nozzle configuration at $M_\infty=2.4$, $\alpha = 0$ -deg, and $C_T = 4.0$



Figure 24 – Sample Schlieren image for the tri-nozzle configuration at $M_\infty = 2.4$, $\alpha = 0$ -deg, and $C_T = 1.0$



Figure 25 – Sample Schlieren image for the tri-nozzle configuration at $M_\infty = 4.6$, $\alpha = 0$ -deg, and $C_T = 1.0$

from a central plenum provides for a lower pressure ratio across the nozzle for the same thrust coefficient and this contributes to a reduction in the standoff distance of the Mach disks and smaller barrel shocks. Apparently having three jets in close proximity to each other contributes to an increase in unsteadiness of the interaction region between the jets, which then causes the bow shock to wiggle periodically. The level of unsteadiness appears to get worse with increasing thrust coefficient for the limited range of data that was acquired. There were a few cases at higher angles of attack where the flow structure switched to being quasi-steady with only occasional bursts of unsteadiness. For the tri-nozzle configuration, an increase in Mach number lead to an general increase in unsteadiness, as shown in Figure 25, a sample image for $M_\infty = 4.6$, $\alpha = 0$ -deg, and $C_T = 1.0$.



Figure 26 – Sample Schlieren image for the quad-nozzle configuration at $M_\infty = 2.4$, $\alpha = 0$ -deg, and $C_T = 1.0$

At angles of attack above 10-deg, even the bow shock became wildly unsteady in certain cases. For comparison, a $M_\infty = 4.6$, $\alpha = 0$ -deg, and $C_T = 1.0$ case is shown in Figure 22 and a $M_\infty = 2.4$, $\alpha = 0$ -deg, and $C_T = 4.0$ case is shown in Figure 23.

Tri-Nozzle

Most of the Priority 1 cases were acquired during the test, with the exception of the highest thrust coefficient and late repeat cases. The Priority 2 and 3 cases of model translations were both dropped.

The tri-nozzle configuration was noticeably more unsteady, in general terms, than the center nozzle, for most of the data acquired. Figure 24 provides the Schlieren image for the tri-nozzle configuration at $M_\infty = 2.4$, $\alpha = 0$ -deg, and $C_T = 1.0$, which allows a direct comparison to Figure 20. The bow shock is closer to the model and slightly less steady than the corresponding center nozzle case. Having three nozzles fed



Figure 27 – Sample Schlieren image for the quad-nozzle configuration at $M_\infty = 2.4$, $\alpha = 0$ -deg, and $C_T = 3.0$

Quad Nozzle

The quad-nozzle configuration was originally Priority 2, however a real-time decision was made by the team that the data would be unique and interesting. Due to time constraints, only two thrust coefficient cases were acquired.

The quad-nozzle configuration provided a mixture of results, with certain cases being noticeably steadier than the tri-nozzle and some not. For instance, at lower thrust coefficients, such as shown in Figure 26 for $M_\infty = 2.4$, $\alpha = 0$ -deg, and $C_T = 1.0$, the flow structure and bow shock are unsteady, as indicated by the slightly irregular bow shock. Increasing the thrust coefficient slightly leads to much steadier conditions. Perhaps this is because the extra nozzle has lowered the pressure ratio closer to the transitional boundary, where the flow structure is generally highly unsteady. Figure 27 provides an example of a higher thrust coefficient quad-nozzle case, with $M_\infty = 2.4$, $\alpha = 0$ -deg, and $C_T = 3.0$. Interestingly, at the higher thrust coefficients, the bow shock tends to flatten out in front of the model. Then, in the region where the flattened bow shock starts to curve, periodic pulsing of the bow shock is typically observed.

5. SUMMARY

Details of the design and development of a new SRP experiment intended as a CFD validation exercise are presented. The LaRC UPWT Test Section 2 was utilized for this test, providing a Mach number range of 2.4 to 4.6. Pre-test CFD solutions were instrumental in sizing and refining the model such that tunnel and internal flow issues would be minimized. A 5-in diameter 70-deg sphere-cone forebody followed by a 10-in long cylindrical aftbody, chosen as a generic shape, was selected for this test based on the results of the CFD study. The forebody allowed for placement of up to four 4:1 area ratio nozzles, with one on the model centerline and three equally spaced at the half radius. The primary instrumentation was high spatial-density surface pressure measurements. High-speed Schlieren video and internal pressures and temperatures were also recorded. A run matrix was developed to allow the quantification of various sources of experimental uncertainty, such as random errors due to run-to-run variations and bias errors due to freestream non-uniformity or model misalignments. Some preliminary results from the wind tunnel entry are presented, although a detailed analysis of the data and uncertainties are still ongoing.

REFERENCES

- [1] Braun, R. D., and Manning, R. M., "Mars Exploration Entry, Descent, and Landing Challenges," *Journal of Spacecraft and Rockets*, Vol. 44, No. 2, 2007, pp. 310–323.
- [2] Steinfeldt, B. A., Theisinger, J. E., Korzun, A. M., Clark, I. G., Grant, M. J., and Braun, R. D., "High Mass Mars Entry, Descent, and Landing Architecture Assessment," AIAA Paper 2009-6684, Sept. 2009.
- [3] Zang, T. A., and Munk, M. M., et al., "Entry, Descent and Landing Systems Analysis Study: Phase 1 Report," NASA TM

2010-216720, July 2010.

- [4] Edquist, K. T., Dyakonov, A. A., Korzun, A. M., Shidner, J. D., Studak, J. W., Tigges, M. A., Kipp, D. M., Prakash, R., Trumble, K. A., Dupzyk, I. C., "Development of Supersonic Retro-Propulsion for Future Mars Entry, Descent, and Landing Systems," AIAA Paper 2010-5046, June 2010.
- [5] Korzun, A. M., and Braun, R. D., "Performance Characterization of Supersonic Retropropulsion for High-Mass Mars Entry Systems," *Journal of Spacecraft and Rockets*, Vol. 47, No. 5, pp. 836-848, 2010.
- [6] Korzun, A. M., Braun, R. D., and Cruz, J. R., "Survey of Supersonic Retropropulsion Technology for Mars Entry, Descent, and Landing," *Journal of Spacecraft and Rockets*, Vol. 46, No. 5, 2009, pp. 929–937.
- [7] Jarvinen, P. O., and Adams, R. H., "The Aerodynamic Characteristics of Large Angled Cones with Retrorockets," NASA CR NAS 7-576, Feb. 1970.
- [8] Trumble, K. A., Schauerhamer, D. G., Kleb, W. L., Carlson, J. R., Buning, P. G., Edquist, K. T., and Barnhardt, M. D., "An Initial Assessment of Navier-Stokes Codes Applied to Supersonic Retro-Propulsion," AIAA Paper 2010-5047, June 2010.
- [9] Aeschliman, D. P. & Oberkampf, W. L., "Experimental Methodology for Computational Fluid Dynamics Code Validation," *AIAA Journal*, Vol. 36, No. 5, 1998, 733-741.
- [10] Oberkampf, W. L. and T. G. Trucano, "Verification and Validation in Computational Fluid Dynamics." *Progress in Aerospace Sciences*. Vol. 38, No. 3, 2002, pp. 209-272.
- [11] Oberkampf, W. L. and Roy, C. J., *Verification and Validation in Scientific Computing*, Cambridge, UK, Cambridge University Press, 2010.
- [12] Jackson, C. M., Jr., Corlett, W. A., and Monta, W. J., "Description and Calibration of the Langley Unitary Plan Wind Tunnel," NASA TP 1905, Nov. 1981.
- [13] Wassum, D. L. and Hyman, C. E. Jr., "Procedures and Requirements for Testing in the Langley Research Center Unitary Plan Wind Tunnel," NASA TM 100529, Feb. 1988.
- [14] Trumble, K. A., Schauerhamer, D. G., Kleb, W. L., and Edquist, K. T., "Analysis of Navier-Stokes Codes Applied to Supersonic Retro-Propulsion Wind Tunnel Test," IEEEAC Paper 1471, March 2011.
- [15] Thermal Desktop User Manual, Cullimore and Ring Technologies, Inc., Version 5.1, October 2007.
- [16] Schwartz, R.J., "ViDI: Virtual Diagnostics Interface Volume 1-The Future of Wind Tunnel Testing" Contractor Report NASA/CR-2003-212667, December 2003.
- [17] Schwartz, R.J., Fleming, G.A., "LiveView3D: Real Time Data Visualization for the Aerospace Testing Environment", AIAA-2006-1388, 44th AIAA Aerospace Sciences Meeting and Exhibit, Reno, Nevada, Jan. 9-12, 2006.
- [18] Schwartz, R.J., McCrea, A.C., "Virtual Diagnostic Interface: Aerospace Experimentation in The Synthetic Environment", MODSIM World 2009 Conference and Expo, Virginia Beach, Virginia, Oct. 14-16, 2009.

BIOGRAPHY

Scott Berry is an aerospace engineer in the Aerothermodynamics Branch at the NASA Langley Research Center. His main area of research has been experimental aeroheating, providing aerothermodynamic support for many recent NASA programs such as Shuttle, X-33, X-34, X-37, X-38, X-43A, and Orion. He has a B.S. in Mechanical Engineering from Worcester Polytechnic Institute and a M.S. in Aeronautics from George Washington University.

Christopher Laws is a mechanical engineer in the Aeronautics Science Engineering Branch at NASA Langley Research Center. He has been involved with the design of several aerospace and aeronautic projects. He has a B.S. in Mechanical Engineering from Virginia Commonwealth University.

Bil Kleb is an aerospace engineer in the Aerothermodynamics Branch at the NASA Langley Research Center. His main area of research has been the development and application of hypersonic computational fluid dynamics codes such as LAURA and FUN3D. He has a long history of providing aerothermodynamic analysis of the Shuttle and has contributed to numerous NASA space access studies such as X-33, X-34, X-37, and Orion. His current research focuses on verification and validation of computational fluid dynamic models to enable prediction of Mars decelerator reentry performance. He has a B.S. and M.S. in Aeronautics and Astronautics from Purdue University, an M.B.A. from the College of William and Mary, and a Ph.D. in Aerospace Engineering from the University of Michigan.

Matt Rhode is an aerospace engineer in the Aerothermodynamics Branch at the NASA Langley Research Center. He has been involved in aerodynamic analysis, characterization, and development for a number of agency programs, including space transportation concepts, planetary systems, and hypersonic cruise vehicles. His current research focuses on powered aerodynamic interactions from propulsion and reaction control systems, such as those on the Orion Launch Abort System and Mars Science Laboratory. He has a B.S. in Aerospace Engineering from Virginia Polytechnic Institute & State University and a M.S. in Aeronautics from George Washington University.

Courtney Spells is an Aerospace Engineer for Jacobs Engineering at the Unitary Plan Wind Tunnel at NASA Langley. Courtney has worked as a wind tunnel test engineer at four of NASA Langley's wind tunnels. She has a B.S. in Aerospace Engineering from Georgia Tech, and has one semester left to get her M.S. in Aerospace Engineering from Georgia Tech.

Andrew McCrea is an aerospace engineer in the Advanced Sensing and Optimal Measurement Branch at

the NASA Langley Research Center. His research focuses on advanced visualization techniques for complex aerospace problems. He has been involved with the development of visualizations for Entry, Descent and Landing, Laser Diagnostics, Ares I/I-X, and Mars Science Laboratory wind tunnel tests. He has been involved with modeling and simulation of Space Shuttle reentry missions for the Hypersonic Thermodynamic Infrared Imaging Team. He has a B.S. in Aerospace Engineering from the University of Maryland, College Park.

Kerry Trumble is an aerospace engineer in the Aerothermodynamics Branch at the NASA Ames Research Center. Her primary focus is in the field of hypersonic computational fluid dynamics, in which she has been involved in the aerothermal analysis of Stardust, Orion Crew Exploration Vehicle, Space Shuttle Damage Assessment and Supersonic Retro-Propulsion. She received her B.S. in Mechanical Engineering from Michigan Technological University and her M.S. in Aerospace Engineering from University of Minnesota, where her thesis was on flow control through laser energy deposition.

Guy Schauerhamer is an aerospace engineer for Jacobs Technology supporting NASA Johnson Space Center's Applied Aeroscience and CFD Branch. He received his B.S. and M.S. in Mechanical Engineering from Utah State University where his thesis was on six-degree-of-freedom moving mesh applications. His primary focus is in the field of computational fluid dynamics, in which he has been involved in the aerodynamic analysis of Mars entry capsules, sounding rockets, Ares V, various Space Shuttle aspects, and supersonic retro-propulsion.

Bill Oberkampf has 41 years of experience in research and development in fluid dynamics, heat transfer, flight dynamics, and solid mechanics. He received his PhD in 1970 from the University of Notre Dame in Aerospace Engineering. He served on the faculty of the Mechanical Engineering Department at the University of Texas at Austin from 1970 to 1979. From 1979 until 2007, he worked in both staff and management positions at Sandia National Laboratories in Albuquerque, New Mexico. During his career, he has been deeply involved in both computational simulation and experimental activities. Many of these activities have been focused on verification, validation, and uncertainty quantification in modeling and simulation. He retired from Sandia as a Distinguished Member of the Technical Staff and is a Fellow of the American Institute of Aeronautics and Astronautics. He has over 160 journal articles, book chapters, conference papers, and technical reports, and co-authored, with Christopher Roy, the book "Verification and Validation in Scientific Computing" published by Cambridge University Press.